IEEE Access
Multidisciplinary | Rapid Review | Open Access Journal

Received December 8, 2020, accepted December 23, 2020, date of publication January 5, 2021, date of current version February 1, 2021.

Digital Object Identifier 10.1109/ACCESS.2021.3049118

Feature Extraction Algorithm Using a Correlation Coefficient Combined With the VMD and Its Application to the GPS and GRACE

YIFAN SHEN[1,2], WEI ZHENG[1,2], WENJIE YIN[2], AIGONG XU[1], AND HUIZHONG ZHU[1]

[1]School of Geomatics, Liaoning Technical University, Fuxin 123000, China
[2]Qian Xuesen Laboratory of Technology, China Academy of Space Technology, Beijing 100094, China

Corresponding authors: Wei Zheng (zhengwei1@qxslab.cn) and Wenjie Yin (wjyin1991@163.com)

This work was supported in part by the National Natural Science Foundation of China under Grant 41774014, Grant 41574014, and Grant 41504010; in part by the Frontier Science and Technology Innovation Project under Grant 085015; in part by the Innovation Workstation Project of the Science and Technology Commission of the Central Military Commission; and in part by the Outstanding Youth Foundation of the China Academy of Space Technology, National Key Research and Development Program of China under Grant 2016YFC0803102.

ABSTRACT To improve the reliability of the Global Positioning System (GPS) and Gravity Recovery and Climate Experiment (GRACE) feature extraction, this paper uses a correlation coefficient combined with the traditional variational mode decomposition (VMD), proposing a new correlation variational mode decomposition (CVMD). In contrast to previous studies, the CVMD denoises the sequences before feature extraction and it is the first time that be used in the GPS and GRACE. First, the correlation between the intrinsic mode function (IMF) and the original sequence is obtained to denoise the original sequence. Moreover, the algorithm reuses the VMD to obtain the IMF components with different frequencies. Then the Lomb Scargle (L-S) spectral analysis and energy density are used to obtain the trend-, seasonal, and residual items. Second, the features of the GPS and GRACE time series are extracted based on the CVMD and multidimensional ensemble empirical mode decomposition (MEEMD) to verify the availability of the CVMD. The results indicate that the CVMD is more superior to the MEEMD in feature extraction. Third, the CVMD is used to extract the trend- and seasonal terms of GPS and GRACE in the North China Plain (NCP). The conclusions are as follows: (1) the seasonal items of GRACE are used to correct the GPS sequences, and the average reduction of the weighted root mean square (WRMS) of each GPS station is 0.69, which demonstrates a strong consistency between the seasonal terms of the GPS sequence and GRACE sequence; (2) during 2003-2015, the mean slope of vertical displacements is 0.20 $\pm$ 0.07 mm / yr, and the uplift rate increases substantially (1.66 $\pm$ 0.62 mm / yr) after 2013. Then, the temporal and spatial relationship between rainfall and crustal load-deformation in the NCP is analyzed, and it is found that the crustal load-deformation is primarily related to rainfall, while human activities play a leading role in the southwestern regions where agricultural irrigation is relatively strong.

INDEX TERMS Correlation variational mode decomposition, feature extraction, GPS, GRACE, North China Plain, vertical displacement of crust.

I. INTRODUCTION

The redistribution and interaction of water reserves causes changes in the surface load, which can lead to a flexible deformation of regional crust in the horizontal and vertical directions [1]. The crustal deformation is primarily divided into structural and non-structural deformations. The structural deformation is caused by the internal tectonic movement of the Earth, manifested by the linear movement of the crust in the horizontal direction ($\boldsymbol{N}$, $\boldsymbol{E}$) [2]. The non-structural deformation is produced by the atmospheric load, snow load, soil water, and other factors [3]. The annual movement leads to seasonal changes in the lithosphere ($\boldsymbol{U}$) [4]. The North China Plain (NCP) is located between the Indian Plate, the Philippine Plate, and the Pacific Plate. The rock structure in this region is uneven in the horizontal and vertical

The associate editor coordinating the review of this manuscript and approving it for publication was Venkata Ratnam Devanaboyina.

directions, which leads to an active crustal movement in the NCP. In recent years, many environmental geological disasters (e.g., land subsidence, seawater intrusion, water quality deterioration) have occurred because of the effects of agricultural irrigation, industrial water, and other activities on water resources [5], [6]. Therefore, it is essential to analyze the seasonal and spatio-temporal characteristics of vertical crustal deformation over the NCP [7], [8].

The Global Positioning System (GPS) has the advantages of high efficiency, all-weather operation, and precision in measurement. Therefore, many scholars use the International Global navigation satellite system Service (IGS) and continuous operating reference stations (CORS) to monitor the crustal deformation in typical region, such as the Asia Europe continent [9], the Himalayas [10] and Southwest China [11], etc. However, the spatial resolution of GPS stations is low, and it cannot cover all regions of the world. In recent years, it has become a research hotspot to improve the spatial resolution of crustal monitoring on the premise of ensuring the accuracy. The launch of GRACE gravity satellites in 2002 ushered in a new era of high-precision gravity field observation [12]. Gravity Recovery and Climate Experiment (GRACE) satellites can monitor changes in water reserves at all depths, including snow, surface water, soil water, and groundwater [13]–[15]. Seasonal changes in water reserves can cause changes in the crustal load, resulting in crustal deformation in the $\boldsymbol{U}$ direction [16]. It is possible to constrain the regional crustal deformation and tectonic dynamic by reconciling the GPS and GRACE [17]–[19]. While, the sequence of GPS and GRACE contain lots of noise signals [20]. It is important to denoise the sequences before feature extraction [21].

To analyze the displacement sequence, the common method is to extract the seasonal and trend-items in the signal using the least square fitting [22], although this method misses the hidden value of the signal. Given this shortcoming, Huang proposed the empirical mode decomposition (EMD) [23]. Then, many scholars utilized the EMD to analysis the $\boldsymbol{U}$ direction sequences of the crust ulteriorly [24]. This method can adaptively extract the seasonal and trend-terms in the signal, while it produces the problems, such as the mode-mixing and end-effect in decomposition [25]. With the optimization of the EMD, the ensemble empirical mode decomposition (EEMD) [26], complete ensemble empirical mode decomposition (CEEMD) [27], variational mode decomposition (VMD) [28], multidimensional ensemble empirical mode decomposition (MEEMD) [29] and other methods are proposed. Although EEMD and CEEMD can effectively suppress the phenomenon of mode-mixing, many computations bring redundant information, and the VMD decomposition method easily solves the problem of end-effect [30]. In recent years, numerous feature extraction methods have been proposed and are based on signal decomposition algorithms and measuring complexity in different fields [31], [32]. The VMD and discrete wavelet transform are utilized to classify the signals [33]. Chen *et al*. proposed a new method based on the normalized mutual information and multiscale to extract the noise features [34]. In addition, Zhang *et al*. combined the nonlocal means (NLM) method with complete ensemble empirical mode decomposition with adaptive noise (CEEMDAN) to denoise the signals [35]. However, there are few studies on denoising the GPS and GRACE sequences. To reduce the effect of noise on decomposition, the new correlation variational mode decomposition (CVMD) feature extraction algorithm is proposed according to the traditional VMD. In this method, the correlation coefficient between the intrinsic mode function (IMF) and the original sequence is used to obtain the denoised signals. It subsequently extracts the features of the denoised secondary signal.

In contrast to previous studies, the CVMD is first proposed and used to extract the trend- and seasonal terms from the sequences of the GPS and GRACE, and the performance of this method is evaluated based on the indexes of the normalized cross-correlation (*NCC*) and signal noise ratio (*SNR*). The seasonal consistency of the GPS and GRACE time series is studied according to the $WRMS_{\text{reduction}}$. Moreover, the precipitation data provided by the China Meteorological Administration (CMA) is used to analyze the spatio-temporal characteristics between the vertical load-displacement and rainfall. This study is significant for the effective management of local water resources and the lives of residents in the NCP.

II. CONSTRUCTION AND EXAMPLE OF THE CVMD

A. PRINCIPE OF VMD

Dragomiretskiy and Zosso proposed the concept of the traditional VMD in 2014 [36], which is different from the non-recursive solution modes such as the EMD, EEMD, and local mean decomposition (LMD). The VMD can effectively eliminate the envelope and over envelope problems by recursion, while it has better adaptability to extract signal features. In the algorithm of VMD, the IMFs are redefined as the elementary amplitude/frequency modulated (AM/FM), modeling the non-stationary and the nonlinearity of the signals [36], as follows:

$$u_k(t) = A_k(t)\cos(\phi_k(t)) \tag{1}$$

where the $\phi_k(t)$ denotes the non-decreasing function; $A_k(t)$ represents the instantaneous amplitude of the $u_k(t)$; t denotes the time of the $u_k(t)$; The $u_k(t)$ has center frequencies and limited bandwidths. Meanwhile, on a sufficiently long interval, the mode $u_k(t)$ can be considered a pure harmonic signal. The IMFs can be extracted by solving the variational problem [36], which is given by:

$$\begin{cases} \min\limits_{y_k,\omega_k} \left\{ \sum\limits_{i=1}^{k} \left\| \partial_t \left[\left(\delta(t) + \dfrac{j}{\pi t} \right) * u_k(t) \right] * e^{-j\omega_k t} \right\|_2^2 \right\} \\ s.t. \sum\limits_{i=1}^{k} u_i(t) = y(t) \end{cases} \tag{2}$$

where j is the imaginary unit; $\delta(t)$ denotes the mean pulse function; t denotes the time of the sequence; k denotes the number of modes; u_k represents the k modes that are decomposed; and ω_k denotes the center frequency of modes. $y(t)$ represents the sequence to be decomposed and ∂_t denotes the first partial derivative of the universal function with respect to time t. $B(t)$ denotes the baseband.

Aiming to solve the optimized question in equation (2), the alternate direction method of multipliers (ADMMs) is used to settle the saddle point. Then, the u_k^{n+1}, ω_k^{n+1}, and λ^{n+1} are updated in the frequency domain [36], as follows:

$$\hat{u}_k^{n+1}(\omega) = \frac{\hat{f}(\omega) - \sum_{i=1}^{k-1} \hat{u}_i^{n+1}(\omega) - \sum_{i=k+1}^{k} \hat{u}_i^{n}(\omega) + \frac{\hat{\lambda}(\omega)}{2}}{1 + 2\alpha(\omega - \omega_k)^2} \quad (3)$$

$$\omega_k^{n+1} = \frac{\int_0^\infty \omega \left|\hat{u}_k^{n+1}\right|^2 d\omega}{\int_0^\infty \left|\hat{u}_k^{n+1}\right|^2 d\omega} \quad (4)$$

$$\hat{\lambda}^{n+1}(\omega) = \hat{\lambda}^{n}(\omega) + \tau(\hat{f}(\omega) - \sum_k \hat{u}_n^{n+1}(\omega)) \quad (5)$$

where the $\hat{f}(\omega)$, $\hat{u}_i(\omega)$, and $\hat{\lambda}(\omega)$ denote the Fourier transform of $f(t)$, $u_i(t)$,and $\lambda(t)$, respectively. Then, the n denotes the iterations, and λ denotes the Lagrangian multiple to render the question unconstrained. The α denotes the balancing parameter of the data fidelity constraint.

In the algorithm of VMD, the low order IMFs denote the slow oscillations (low-frequency modes), and the high order IMFs denote the fast oscillations (high- frequency modes). Therefore, the original sequence $y(t)$ is decomposed into k modes as follows:

$$y(t) = IMF_1 + IMF_2 + \cdots + IMF_k \quad (6)$$

B. DEVELOPMENT OF CVMD

The traditional VMD still brings about heavy losses of accuracy in the process of sequence feature extraction because of the influence of high-frequency noise. Therefore, this study combines the correlation with the traditional VMD for the first time namely CVMD. To avoid over or under decomposition, the CVMD determines the number of IMFs (k) through the center frequency of the component. The correlation between each component and the original sequence is calculated, and the weak correlation and uncorrelated IMFs are removed. The remaining rest components are reconstructed to produce denoised sequence. Then, this algorithm uses the denoised sequence as the input data to decompose and extract the feature sequence. The structure of the CVMD is shown in Figure 1. The elaboration of the CVMD is shown as follows.

1) OBTAIN THE DE-NOISED SEQUENCE

To reduce the influence of noise on feature extraction, the proposed method uses the correlation coefficient between each mode and the original sequence, and it removes the uncorrelated and weak correlation components. The process of solving for the correlation coefficient is shown in the following formula:

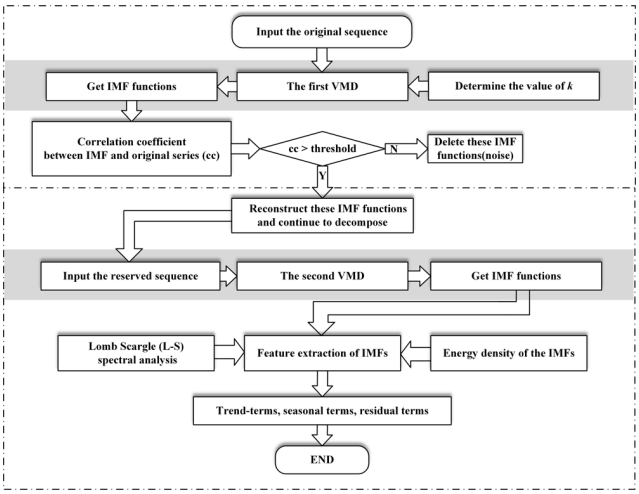

FIGURE 1. The Flow chart of the Correlation variational mode decomposition.

$$R_i = \frac{\mathrm{Cov}[y(t), IMF_i]}{\sqrt{\mathrm{Var}[y(t)] \times \mathrm{Var}[IMF_i]}} \quad i = 1, 2, \cdots, k \quad (7)$$

where R_i denotes the correlation coefficient; $y(t)$ represents the original sequence; and IMF_i is the decomposed components. According to the value of R_i, we can judge the correlation between the mode and the original function. The general correlation and strong correlation components are reconstructed, while the uncorrelated and weak correlation components should be removed. Table 1 describes the correlation coefficient and correlation correspondence [37].

TABLE 1. The relationship between the correlation coefficient (R_i) and correlation.

	No Correlation	Weak Correlation	Moderate Correlation	Strong Correlation
R_i	0 ~ 0.1	0.1 ~ 0.3	0.3 ~ 0.5	0.5 ~ 1

This paper determines the threshold of cc based on the energy spectrum index of the IMFs. The noise signals could be removed. Meanwhile, the correlation coefficient will be counted. Through abundant simulation experiments, the cc threshold is fixed at 0.3 in this paper [28]. Then, the denoised sequence is obtained, and its expression is as follows:

$$y(t)_{\mathrm{denoise}} = \sum \mathrm{IMF}_i, \quad (i|0.3 < R_i < 1) \quad (8)$$

where $y(t)_{\mathrm{denoise}}$ denotes the reconstructed sequence after denoising; n denotes the number of satisfied sequences; and R_i denotes the correlation coefficient between the modes and the original sequence.

2) THE SECOND DECOMPOSITION

After the denoised sequence is obtained, $y(t)_{\text{denoise}}$ is taken as the initial input sequence. The seasonal and trend-items can be obtained according to the above decomposition method. Then the Lomb Scargle (L-S) spectral analysis and energy density are used to obtain the trend-, seasonal, and residual items [38], [39]. The extraction results are as follows:

$$y(t)_{\text{denoise}} = IMF_{\text{SEA}} + IMF_{\text{TRE}} + \varepsilon \tag{9}$$

where IMF_{SEA} denotes the seasonal term of the series extracted from the CVMD; IMF_{TRE} denotes the feature of the trend-item obtained from profit extraction; and ε is the residual noise sequence.

III. EXPERIMENTAL VERIFICATION OF THE CVMD

A. DATA AND MODELS

1) GPS DATA AND PREPROCESSING

There are 10 CORS stations in the NCP, which are provided by the Crustal Movement Observation Network of China (Figure 2a). Figure 2b manifests the relationship between the GPS sites and GRACE grids in the NCP. The coordinate datasets of CORS, such as the ionospheric correction, absolute antenna phase center correction, and ocean tide correction, are corrected by the GAMIT. The baseline among stations is calculated based on the GLOBK. Furthermore, the sequences' outliers threefold larger than the standard deviation are removed to weaken the influence of abnormal values. Given the inconsistency of the time series span between the GPS and GRACE, this study selects the most extended time series of the GPS and GRACE for analysis. The periods of the CORS stations are 2010-2015, except BJFS and BJSH (2003-2015) [40].

2) GRACE DATA AND INVERSION MODEL

The mass changes can deform the displacement of the crust of the Earth. The surface water, atmosphere and non-tidal ocean loads lead to the load-deformation, and especially contribute to the vertical crustal non-tectonic movement [41]. The load-deformation can be estimated using the GRACE spherical harmonic (SH) coefficients based on the theory of elastic load-deformation [42] as follows:

$$\Delta h(\theta,\varphi) = A \times \sum_{l=0}^{\infty}\sum_{m=0}^{1} \frac{h_l}{1+k_l} \times W_l \times \overline{P}_{l,m}(\cos\theta) \times [\Delta C_{lm}\cos(m\varphi) + \Delta S_{lm}\sin(m\varphi)] \tag{10}$$

where A is the radius of the Earth (6371.393 km); h_l and k_l represent the load Love number of order l; W_l denotes the kernel function of Gaussian smoothing; $\overline{P}_{l,m}$ represents fully normalized Legendre functions of degree l and order m; ΔC_{lm} and ΔS_{lm} are the variation of spherical harmonic coefficient of the Earth's gravitational field.

The C20 terms are replaced by the satellite laser ranging (SLR) data of the five geodetic satellites (LAGERS-1 and 2, Stella, Starlette, and Ajisai) [43]. Because the GRACE gravity field cannot determine the degree-1 terms, this study replaces these terms with the results derived by Swenson *et al.* [44]. We use the Gaussian smoothing with an average radius of 300 km to deduct the error of the North-South strip. Because the influence of the non-tidal factors of atmosphere and ocean, the GAC correction is added to the spherical harmonic coefficient. Finally, to better compare and analyze with the GPS sequences, first-order correction processing should be performed for the calculation results [45].

The GRACE observations are provided by the Center for Space Research (CSR), Geo Forschungs Zentrum (GFZ), and the Jet Propulsion Laboratory (JPL). The scaling factor method is used to recover the signalized leakage generated by filtering. The uncertainty of the GRACE signal is quantified according to the three-cornered hat (TCH) [46], and the mean value of the three time-series is taken as the result, as shown in equation (9):

$$\Delta\overline{h} = \frac{\Delta h_{\text{CSR}} + \Delta h_{\text{GFZ}} + \Delta h_{\text{JPL}}}{3} \tag{11}$$

B. EVALUATION INDEX

To demonstrate the superiority of the CVMD, two indicators (i.e., *NCC* and *SNR*) are used to evaluate the similarity and denoising effect of the extracted feature sequence and the original sequence [47].

1) NCC

The calculation formula of *NCC* is as follows [48]:

$$NCC = \sum_{n} \frac{1}{\sigma_f \sigma_h}(f(n) - \mu_f)(h(n) - \mu_h) \tag{12}$$

where $f(i)$ and $h(i)$ represent the original sequence and the reconstructed sequence, respectively; i represents the number of the sequence; n represents the number of sampling points in the sequence; and σ and μ represent the standard deviation and mean value of the sequences, respectively. The value of *NCC* is between - 1 and 1. When the value of *NCC* is equal to 1, the signals of the two sequences are identical. Therefore, the closer the *NCC* value is to 1, the more similar the information contained between the reconstructed and original signals is [49].

2) SNR

The calculation formula of the *SNR* is as follows [48]:

$$SNR = 10 \times \lg \frac{\sum_{i=1}^{N} f^2(i)}{\sum_{i=1}^{N} [f(i) - g(i)]^2} \tag{13}$$

where N denotes the number of sampling points in the sequence; $f(i)$ denotes the sequence of the feature; and $g(i)$ denotes the original sequence. The more substantial *SNR* value is, the less noise content is in the sequence, and the more obvious the denoising performance is [50].

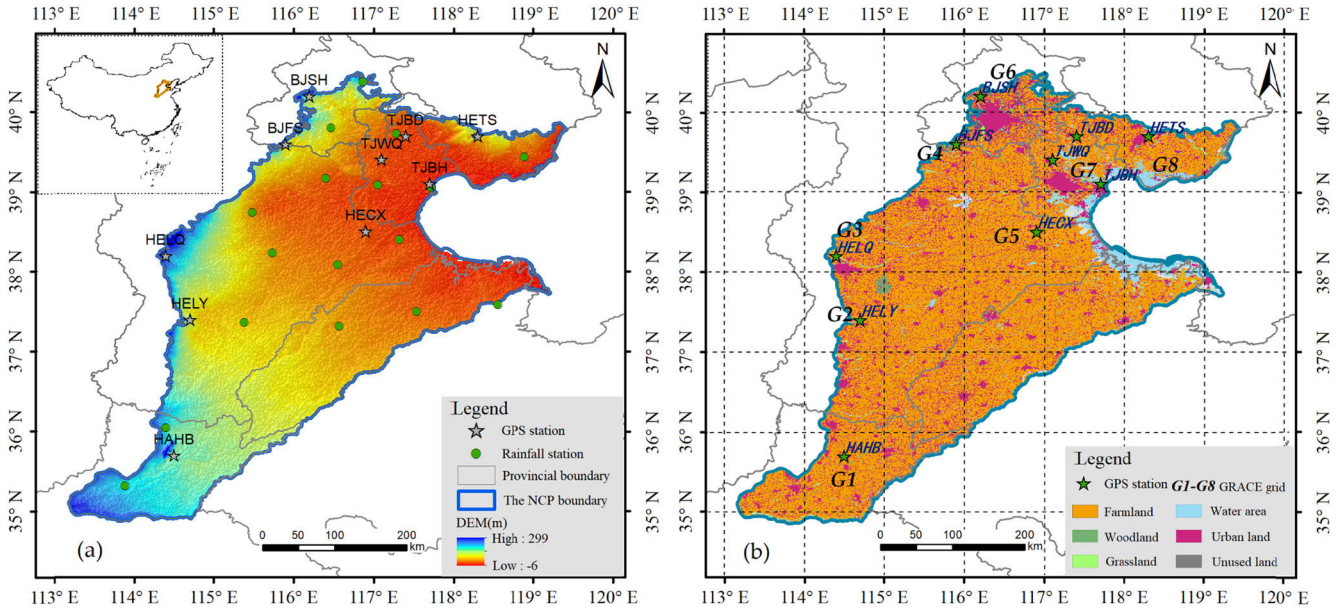

FIGURE 2. (a) The distribution of CORS stations (green stars) and meteorological stations (green dots) in the NCP. (b) The relationship between the CORS stations (green stars) and GRACE grids (the red 'G1-G8'), the background represents the use of land in the NCP.

C. VERIFICATION OF THE CVMD

The study verifies the validity and reliability of the CVMD based on the time-series of the GPS and GRACE. The datasets of the GPS and GRACE are provided at daily and monthly resolutions, separately. Moreover, the CVMD is compared with the MEEMD to indicate the advantages of feature extraction.

The CVMD is used to pre-decompose the sequences, using the BJFS station (GPS) as an example. To determine the decomposition number k, the usual method is to adopt different values of k to decompose the original signal. The decomposition number k is determined by analyzing the center frequency value of the decomposed mode. If there are modes with similar center frequencies, then VMD over decomposition should be considered. Therefore, we should compare the center frequency of IMF_k and IMF_{k-1}, and the test will be stopped when the center frequency of IMF_k approximately equal to IMF_{k-1} [51]. Moreover, the other parameters of alpha, tau, DC, initialization, and tolerance are equal to 2500, 0, 1, 1, and 1e-6, separately. The calculation results of the center frequencies of the IMF components are shown in Table 2.

As shown in Table 2, the center frequency of IMF5 approaches that of IMF6 when k equals 7. The center frequencies of IMF5 and IMF6 are very close when k equals 8. Moreover, the center frequencies of IMF7 and IMF8 are also almost identical. These results indicate that there is a phenomenon of a false mode when k is not less than 7. To sum up, 6 is the most appropriate parameter in this experiment, and the value of alpha, tau, DC, initialization, and tolerance are equal to 2500, 0, 1, 1, and 1e-6, separately. The result of pre-decomposition is shown in Figure 3.

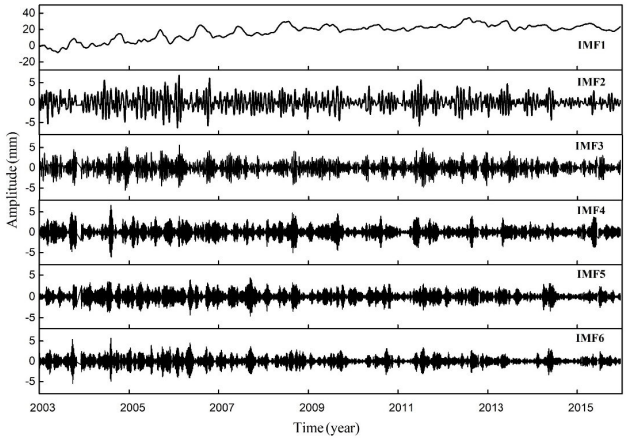

FIGURE 3. The pre-decomposition effect chart based on the CVMD in BJFS GPS station.

The correlation coefficient (R_i) between each IMF and the original sequence is calculated. Moreover, the IMF within 0 to 0.3 is removed, and the remaining IMFs are reconstructed to achieve the denoising effect (Figure 4).

Figure 4 shows that the correlation coefficient between IMF1 and the original sequence is higher than 0.3. This result shows that IMF1 has a strong correlation with the original signal. However, the correlation coefficients between the remaining IMF components and the original sequence are all less than the threshold, indicating a weak correlation attribute with original signals. Thus, IMF1 is retained as the denoised sequence for the following decomposition. The GPS sequence is denoised to obtain the input sequence of the secondary decomposition based on the CVMD, and the processing results are shown in Figure 5.

TABLE 2. Central frequency values of IMs with different *k* values.

k	IMF1	IMF2	IMF3	IMF4	IMF5	IMF6	IMF7	IMF8
k=1	6.23E-02	---	---	---	---	---	---	---
k=2	5.87E-02	7.62E+02	---	---	---	---	---	---
k=3	5.20E-02	9.41E+02	3.42E+03	---	---	---	---	---
k=4	4.90E-02	6.25E+02	1.71E+03	4.00E+03	---	---	---	---
k=5	7.50E-02	5.73E+02	1.50E+03	2.73E+03	4.07E+03	---	---	---
k=6	6.60E-02	5.02E+02	1.22E+03	1.96E+03	2.93E+03	4.11E+03	---	---
k=7	6.70E-02	4.32E+02	9.57E+02	1.72E+03	3.15E+03	3.19E+03	4.11E+03	---
k=8	7.90E-02	3.59E+02	8.14E+02	1.41E+03	3.04E+03	3.05E+03	3.95E+03	4.15E+03

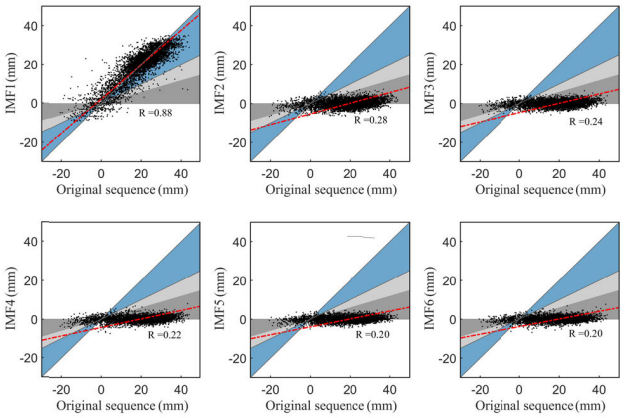

FIGURE 4. The correlation coefficients between IMF components and the original sequence (the value of R); *N* denotes the number of points; the shades of dark gray, light gray, and blue express the ranges of the correlation coefficients, which are 0-0.3, 0.3-0.5, and 0.5-1; the red dotted lines denotes the regression equations.

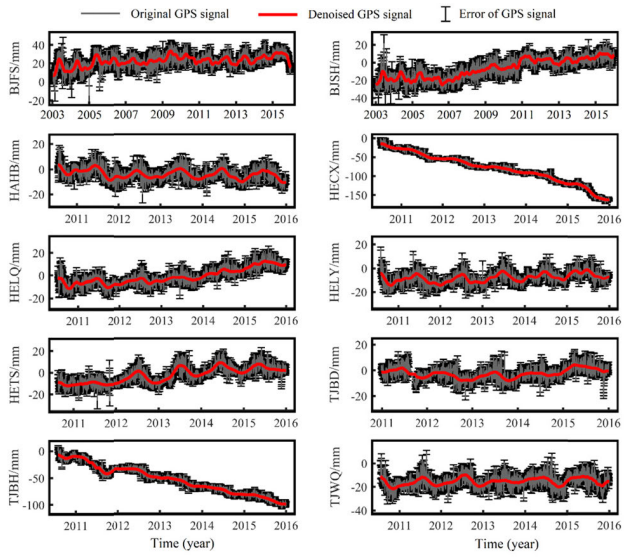

FIGURE 5. The denoising effect based on the CVMD; the grey lines denote original GPS signals, the black I-shapes represent the error of GPS signals, and the red lines denote the denoised GPS signals.

Figure 5 indicates that the denoised sequence is smoother than the original sequence. Moreover, the denoised sequence continues to be the input sequence, and the steps of decomposition are repeated to obtain the feature components of different frequencies. The parameters of the second decomposition are shown in Table 3. To verify the reliability of the CVMD, the MEEMD feature extraction method was used as the control experiment, and *NCC* and *SNR* are used as the evaluation indices. The feature extraction results of the two methods for the BJFS station are shown in Figure 6 and Figure 7.

TABLE 3. The parameters of the second VMD, it includes the alpha, k, tau, DC, initialization, and tolerance.

Parameter	*alpha*	*tau*	*k*	*DC*	*initialization*	*tolerance*
Value	2500	0	10	1	1	1e-6

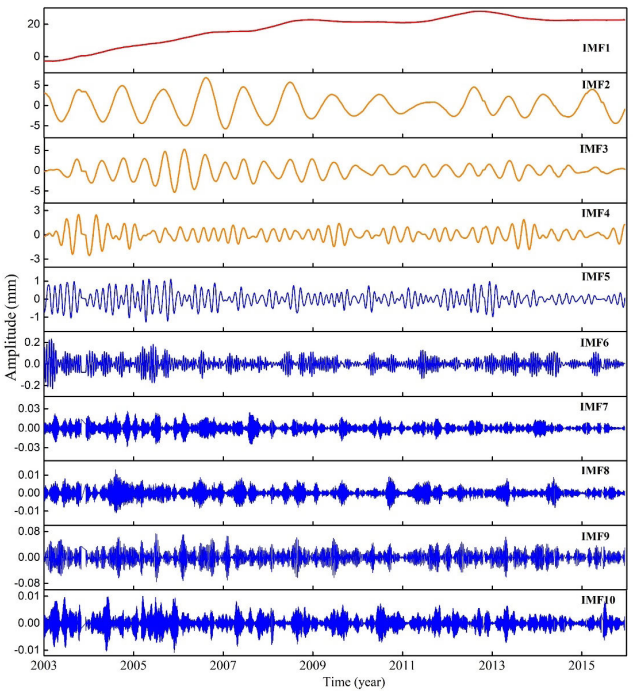

FIGURE 6. Decomposed results based on the CVMD. IMF1, IMF2 - IMF4, and IMF5 - IMF10 denote the trend-term, seasonal term, and noise-term [52] extracted by the CVMD, respectively.

The characteristics of the sequence are distinguished using L-S spectrum analysis and the energy density of the

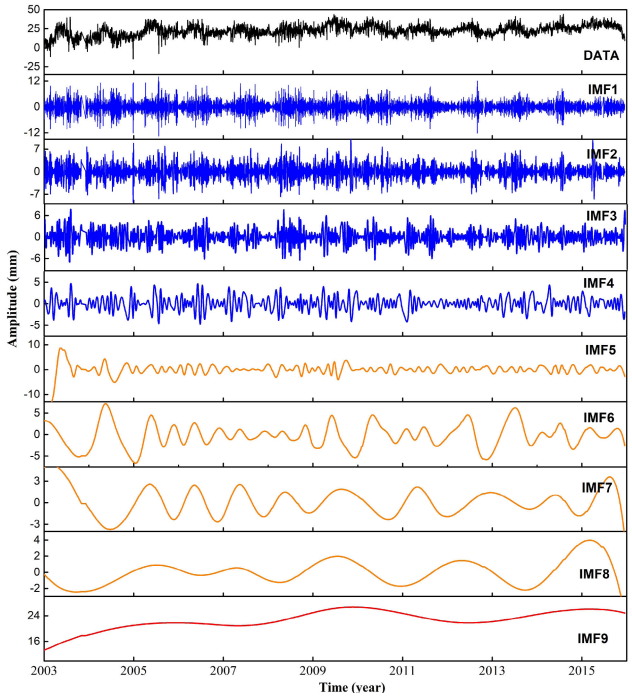

FIGURE 7. Decomposed results based on the MEEMD. IMF1-IMF4, IMF5-IMF8, and IMF9 representing the residual, seasonal and trend-items extracted from the MEEMD, respectively.

components [53]. Figure 6 shows the result of sequence feature extraction by the CVMD. A small amount of noise remains in the second decomposition, but the amplitude of the noise is far smaller than that of the original sequence. This result indicates that the noise has a slight effect on the sequence currently. Figure 7 indicates that the MEEMD also has the ability of sequence feature extraction. However, the amplitude of its noise part is large, indicating that the noise has a greater effect on the sequence feature extraction process through the MEEMD. With regard to distinguishing the abilities of the two feature extraction methods, this paper compares the trend -term and seasonal term of the extraction results.

1) COMPARISON OF TREND-CHARACTERISTICS

In this section, the CVMD is used to extract the trend-terms of the GPS and GRACE sequences, and the slope values of the trend -sequences are shown in Table 4. The slope values of the trend -terms and original sequences are compared to express the advantage of trend-term extraction. If the trend-term is closer to the slope value of the original sequence, the extraction result is more reliable.

Table 4 indicates that the CVMD is more reliable and stable than the MEEMD. After statistical analysis, the accuracy of the CVMD method is 84.41% in the trend extraction of the GRACE sequence, higher than that of the MEEMD (74.12%). In terms of the trend-feature extraction of the GPS sequence, the accuracy of the CVMD method is 97.87%, which is higher than 92.39% for the MEEMD. The above observations show that the CVMD outperforms the method of MEEMD.

2) COMPARISON OF SEASONAL CHARACTERISTICS

The performance of the CVMD and MEEMD are compared regarding extracting the seasonal terms. The original sequence is compared from the frequency domain by drawing the superposed power spectrum. This comparison adequately explains the relationship between the reconstructed sequence and the original sequence obtained by these two decomposition methods [54]. The BJFS station is chosen as an example to show the superimposed power spectrum of the seasonal characteristics (Figure 8).

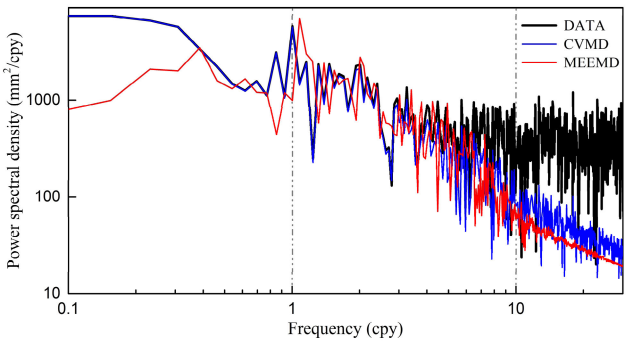

FIGURE 8. The seasonal superposed power spectrum of the BJFS station based on the CVMD (blue line) and MEEMD (red line). The black line denotes the power spectral density of the original data.

Figure 8 shows that the seasonal term of the CVMD agree with the original sequence, while the MEEMD extraction result differs from the original sequence. The sequence separated by the CVMD in the high-frequency part is different from the original sequence. Moreover, the result of the MEEMD is different from the original sequence. The CVMD effectively extracts the seasonal terms in the sequence. The *NCC* and *SNR* are used to demonstrate the superiority of the CVMD, the results are shown in Table 5 [48].

Table 5 shows that the results of the CVMD are substantially better than those of the MEEMD. Further statistical results for Table 5 are as follows: (1) In the seasonal term extraction of the GRACE, the average *NCC* value of the CVMD is 0.79, while that of MEEMD is 0.62, an average increase of 27.42%. Moreover, the mean the *SNR* of CVMD and MEEMD are 6.96 and 3.83, respectively. (2) In the seasonal term extraction of the GPS, the mean *NCC* value of the CVMD is 0.86, while that of the MEEMD is 0.64, an average increase of 34.38%. Moreover, the mean *SNR* result of the CVMD and MEEMD are 16.56 and 10.13, respectively. The above statistical results show that the CVMD is more accurate than the MEEMD in the extraction of seasonal term.

3) THE ROBUSTNESS TEST

In order to text the robustness of the threshold, this study has calculated the correlations between the IMFs and the original signals. the results are shown in the Table 6.

Table 6 shows that the value 0.3 is enough to denoised the noisy IMFs. However, if the threshold is 2.9, the robustness

TABLE 4. The results of sequence trend-feature extraction based on the CVMD and EMD, Ori-seq denotes the original sequence.

GRACE grids	Slope (mm/yr)			GPS sites	Slope (mm/yr)		
	Ori-seq	CVMD	MEEMD		Ori-seq	CVMD	MEEMD
G1	0.21	0.20	0.19	HAHB	-0.79	-0.76	-0.66
G2	0.23	0.21	0.20	HELY	1.08	1.07	1.03
G3	0.09	0.11	0.07	HELQ	3.71	3.66	3.27
G4	-0.02	-0.03	-0.01	BJFS	0.74	0.75	0.65
G5	0.11	0.10	0.08	HECX	-23.69	-23.04	-22.56
G6	-0.10	-0.08	-0.07	BJSH	2.56	2.56	2.49
G7	-0.08	-0.08	-0.06	TJBD	0.67	0.69	0.63
				TJBH	-16.33	-15.19	-14.47
				TJWQ	0.52	0.52	0.50
G8	-0.10	-0.11	-0.07	HETS	3.44	3.40	3.36

TABLE 5. Sequence seasonal feature similarity and signal-to-noise ratio based on the CVMD and MEEMD.

GRACE grids	*NCC*		*SNR* (dB)		GPS sites	*NCC*		*SNR* (dB)	
	CVMD	MEEMD	CVMD	MEEMD		CVMD	MEEMD	CVMD	MEEMD
G1	0.84	0.76	8.19	3.64	HAHB	0.78	0.57	7.41	4.45
G2	0.79	0.63	9.07	5.22	HELY	0.77	0.43	9.19	5.63
G3	0.86	0.52	5.58	3.16	HELQ	0.92	0.85	12.80	7.56
G4	0.69	0.47	5.97	2.54	BJFS	0.80	0.52	13.34	8.65
G5	0.84	0.62	7.21	4.47	HECX	0.96	0.63	34.05	15.63
G6	0.69	0.59	6.87	3.51	BJSH	0.78	0.61	11.82	5.66
G7	0.82	0.72	6.56	3.69	TJBD	0.93	0.75	5.53	4.37
					TJBH	0.98	0.78	28.80	18.79
					TJWQ	0.89	0.61	34.15	25.73
G8	0.79	0.63	6.25	4.41	HETS	0.81	0.63	8.49	4.82

TABLE 6. The results of the correlations between the IMFs and the original signals, the Purple row is the name of the GPS signal, the Blue row is the denoised part (as the input data for the second VMD) of the IMFs, and the Grey rows represent the noisy IMFs of the original signals (distinguished by the energy density).

Correlations	IMF1	IMF2	IMF3	IMF4	IMF5	IMF6
BJFS	0.882	0.284	0.235	0.221	0.199	0.203
BJSH	0.769	0.298	0.285	0.254	0.232	0.211
HAHB	0.909	0.216	0.199	0.177	0.148	0.138
HECX	0.691	0.286	0.271	0.262	0.259	0.230
HELQ	0.995	0.062	0.050	0.041	0.035	0.036
HELY	0.881	0.260	0.232	0.184	0.163	0.151
HETS	0.681	0.296	0.287	0.272	0.269	0.246
TJBD	0.854	0.296	0.246	0.190	0.178	0.170
TJBH	0.674	0.292	0.281	0.271	0.258	0.221
TJWQ	0.989	0.098	0.070	0.056	0.052	0.052

of the threshold is 50% (BJFS, HETS, TJBD, TJSH, and TJWQ signals are not satisfy the 0.29). When the threshold equals 0.31, the robustness also can denoised the noisy IMF. If the threshold over 0.3, it may remove the useful IMFs (high-correlation). However, there are quite different for the thresholds of the useful and noisy IMFs.

Aiming to verify the robustness of the threshold (0.3), we have simulated 100 signals according to the real GPS signals. We have calculated the robustness of the threshold; it shows that the threshold (0.3) is enough to denoised the signals. Meanwhile, the robustness of the 0.29 is 84%.

IV. APPLICATION OF THE CVMD

A. COMPARATIVE ANALYSIS OF GPS AND GRACE MONITORING RESULTS

The CVMD is used to separate the trend-term and seasonal terms of the GPS and GRACE time-series. Table 4 and Figure 9 describe the trend- and seasonal items, respectively.

Figure 9 shows that there are differences between the phase and amplitude of crustal deformation (GPS) and crustal load-deformation (GRACE) in the NCP. The amplitude of the crustal deformation sequence is between 2.3 mm and 9.8 mm, while the load-deformation ranges from 2.1 mm to 5.2 mm. Above all, the amplitudes of the GPS are larger than those of the GRACE. The crustal load-deformation shows a substantial seasonal change, and groundwater is primarily

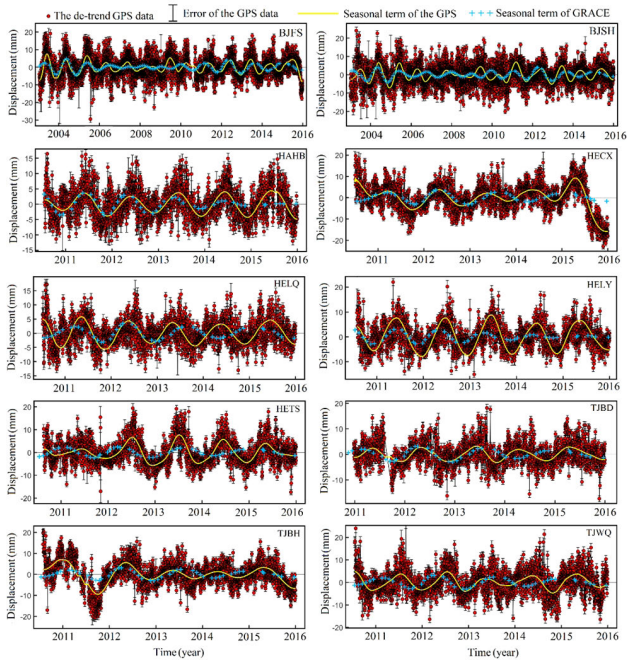

FIGURE 9. The seasonal term extraction effect of the GPS (yellow lines) and GRACE vertical series (blue points) in the NCP based on the CVMD. The red points represent the GPS data that de-trended.

used for agricultural irrigation at the end of the spring and summer. The remaining rainwater is stored in the spring of the second year except for evaporation and runoff. Therefore, the crustal load -deformation in the spring shows a negative state.

To verify the consistency of the GPS and GRACE in seasonal terms, the quantitative analysis of the weighted root mean square (WRMS) is used as follows [55]:

$$WRMS_{\text{GPS}} = \sqrt{\frac{1}{n} \times \sum_{i=1}^{n} \frac{1}{\sigma^2} \times c_i} \tag{14}$$

$$WRMS_{\text{GPS-GRACE}} = \sqrt{\frac{1}{n} \times \sum_{i=1}^{n} \frac{1}{\sigma_i^2 + \sigma_{Gi}^2} \times (c_i - \Delta h_i^G)^2} \tag{15}$$

where n denotes the number of solutions per -day; c_i denotes the sequence after the detrend -item; σ denotes the standard deviation; and Δh_i^G denotes the time series of removing the GRACE by the GPS.

After calculating the *WRMS* based on the above formula, the experiment calculates the GPS sequences after deducting the self-fitting $WRMS_{\text{GPS}-\text{GPSfit}}$. Moreover, the following formula is used to quantitatively evaluate the percentage reduction *WRMS* of the GPS station [56]:

$$WRMS_{\text{reduction}} = \frac{WRMS_{\text{GPS}} - WRMS_{\text{GPS-GRACE}}}{WRMS_{\text{GPS}} - WRMS_{\text{GPS-GPSfit}}} \tag{16}$$

where $WRMS_{\text{reduction}}$ shows the relationship among sequences in terms of the period, amplitude, and phase. When the value of $WRMS_{\text{reduction}}$ equals 1, the seasonal parameters of the two fitting methods are coincident. Figure 10 shows the value of each station calculated using the above formula.

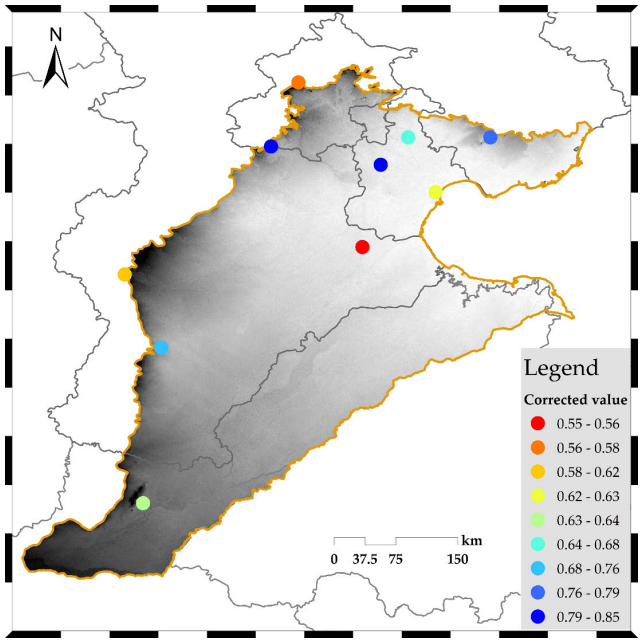

FIGURE 10. *WRMS* correction value after the GRACE corrected GPS sequence (the points).

Figure 10 shows that each value of $WRMS_{\text{reduction}}$ is above 0.5, and the average corrected value in 10 GPS stations is 0.69. Moreover, the *WRMS* corrections of BJFS, TJWQ and HELY are more than 0.7. This result shows that the seasonal characteristics of the GPS match well with the GRACE, and using GRACE is effective for correcting the GPS.

B. TEMPORAL AND SPATIAL FEATURE OF CRUSTAL LOAD-DEFORMATION IN THE NCP

The vertical load-deformation of the crust is primarily related to the water resource reserves. When the amount of water increases, the crust produces vertical deformation downward. In contrast, it leads to the crustal rebound. The precipitation product is used to analyze the cause of load-deformation in the NCP. The trend-signals of crustal deformation in various periods are retrieved via GRACE using the CVMD, and the results are shown in Figure 11.

Figure 11 shows that the crustal load -deformation increased at the rate of 0.20 $\pm$ 0.07 mm/yr during the 13 years study period. The seasonal fluctuation of crustal deformation is closely related to the rainfall. When there is more rainfall in the summer, the deformation of the Earth's crust is in a trough. The deformation gradually rebounds with a decrease in rainfall, and there is a lag of 2 months in phase. During 2013-2015, the crustal load-deformation showed an obvious uplift trend, with a slope of 1.66 $\pm$ 0.62 mm/yr. The rainfall was substantially lower than average for many years, indicating that the variation of rainfall has an essential effect

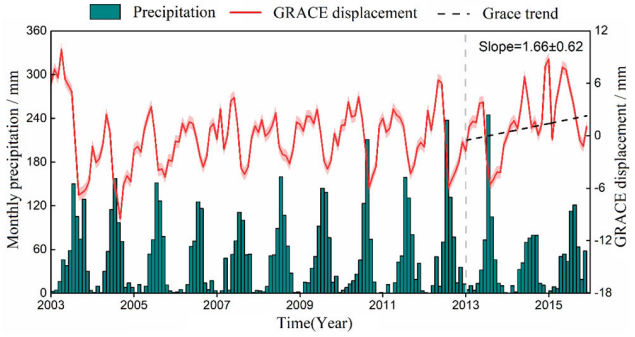

FIGURE 11. Time series of crustal non-structural deformation (red line) and monthly precipitation (green column) in the NCP.

on the crustal deformation of the NCP. The findings of this study show good consistency with previous research [57].

In practice, the real land water reserves are difficult to obtain, and organizations adopt different data processing strategies and background models [58]. There are some differences in the phase, amplitude and period characteristics of inversion shape variables [59]. Therefore, it is difficult to evaluate the uncertainty of the inversion results of the GRACE. Unlike the traditional error estimation method, the TCH used in this paper can evaluate the uncertainty of more than three sets of observation sequences (Δh_{CSR}, Δh_{GFZ}, Δh_{JPL}, and $\Delta \bar{h}$) without knowing the real reference field [60]. The error of the crustal deformation is estimated as ∼0.71 mm in the entire NCP, as shown in the shaded region of Figure 11.

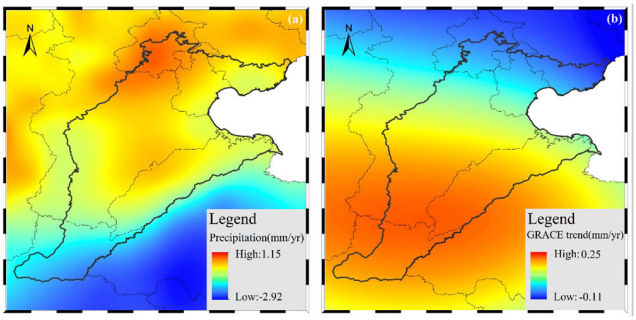

FIGURE 12. Long-term trends of (a) monthly precipitation and (b) load-deformation from 2003 to 2015 in the NCP.

Figure 12 represents the temporal and spatial relationship between rainfall and load-deformation in the NCP from 2003 to 2015. Over this period, the rainfall increased substantially in the northern regions in the southern regions (Figure 12a). The decrease in the water supply leads to the apparent vertical uplift of the crust (Figure 12b), indicating that rainfall has a substantially contribution to the crustal load-deformation. However, the lowest point of the rainfall decreasing trend appears over the southern region of the NCP (Central of Shandong Province), while the region with the fastest rate of crustal uplift is the southwest region over the NCP (Henan Province). The difference between Figure 12a and Figure 12b shows that agricultural irrigation may play a leading role in the vertical displacement of the southwest.

V. DISCUSSION

Because of the influence of various factors on the crustal deformation (GPS and GRACE), the crustal deformation sequence is full of noises. These noises have a certain effect on the feature extraction of the crustal deformation sequence, so it is necessary to remove them before feature extraction. The correlation coefficient is used to remove the noise components based on the traditional VMD to obtain the clean sequence. Finally, the denoised sequence is decomposed twice to obtain the characteristic sequence of the sequence, which is discussed in Section II.

The crustal displacements are calculated based on the data of the GPS signals (Figure 2) and the data of the GRACE. Equation (10) estimates the load- deformation based on the GRACE spherical harmonic coefficients. The CVMD is used to extract the features of the GPS and GRACE sequences and compare them with the MEEMD (Section 3.3). The results show that the slope of the trend-feature extracted by the CVMD is closer to the original sequence than that of the MEEMD (Table 4), and the seasonal feature is better than that of the MEEMD in *NCC* and *SNR* (Table 5). This study uses the CVMD to decompose the GPS and GRACE signals (Figure 9) in the NCP, and the consistent characteristics between the GPS and GRACE are calculated using Equations (15) and (16). Finally, the temporal and spatial variation between load -deformation and rainfall is analyzed. The results play an important role in the effective management of water resources in this region (Section IV).

One may wonder why the CVMD is proposed when the EMD, EEMD, MEEMD, and other methods can decompose the sequence to obtain the characteristic components of different frequencies. First and foremost, a single traditional method cannot avoid the effect of sequence noise on feature extraction. In addition, the method can also make the sequence smoother and can show the trend, amplitude, and phase of the sequence more clearly. However, there remain some shortcomings in this method, such as the small amount of high-frequency noise in the high-frequency part of the result of the secondary decomposition of the sequence. The amplitude of these noises is smaller than the original sequence, but it will also have a certain effect. Therefore, in the follow-up study, the high-frequency of the sequence component will be added. After the threshold is set, the noise is extracted more thoroughly.

VI. CONCLUSION

It is important to improve the reliability of the feature extraction of the GPS and GRACE nonlinear discrete sequences. The accuracy of the extraction determines the reliability of the geophysical analysis. Aiming at the shortcomings of existing feature extraction methods, the correlation coefficient is used to weaken the effect of noise in the CVMD.

1) This study considers the correlation coefficient between the IMF and the original sequence based on the traditional VMD to remove the noise component.

The denoised sequence is decomposed and reconstructed to achieve feature sequence acquisition.

2) The CVMD and MEEMD are used to extract the feature items of the GPS and GRACE original sequences. The results indicate that the CVMD is more reliable and stable than the MEEMD. The accuracy of CVMD is 97.87% for the trend-feature extraction of GPS and 84.41% for the GRACE sequence, which is higher than 92.39% and 74.12%, respectively, for MEEMD feature extraction. These results suggest that the CVMD outperforms the MEEMD decomposition method.
3) In the extraction of the seasonal feature, the average *NCC* of the CVMD is 0.83, which is 30.90% higher than that of the MEEMD; the *SNR* of CVMD is 11.76, which is higher than 6.98 for the MEEMD. These results indicate that the feature extraction method of CVMD has the characteristics of a strong similarity and high signal-to-noise ratio, which shows that the results of feature extraction are more reliable than those of the MEEMD.
4) The seasonal characteristics of the GPS and GRACE sequences in the NCP are extracted by the CVMD. The results indicate that the GPS signal has a slightly larger amplitude than that of the GRACE signal, and there is a phase difference, which may be caused by the slow deformation of the hydrological load. The $WRMS_{\text{reduction}}$ of the GPS is used to evaluate the relationship between the GPS and GRACE series. The mean $WRMS_{\text{reduction}}$ value of 10 GPS stations is 0.69. The results indicate that the seasonal terms of the GPS and GRACE are well correlated, and it is effective to correct the GPS by means of the GRACE observations.
5) Finally, the crustal load-deformation of the NCP was uplifted vertically at a rate of 0.20 ± 0.07 mm/yr from 2003 to 2015. Because of the decrease of rainfall in the southern regions, the decrease in the water supply leads to the vertical uplift. However, human activities play an essential role in crustal load-deformation in the farming regions.

ACKNOWLEDGMENT

The authors greatly appreciate China Earthquake Administration for the GPS data of Crustal Movement Observation Network of China (CMONOC) and the three institutions (CSR, JPL, and GFZ) that provide the GRACE data. They also thank that the data of precipitation is provided by the CMA. *(Yifan Shen, Wei Zheng, and Wenjie Yin contributed equally to this work.)*

REFERENCES

[1] G. Dagan, "Solute transport in heterogeneous porous formations," *Water Resour. Res.*, vol. 55, no. 3, pp. 671–682, 2004.
[2] X. Wang, L. Chen, Y. Ai, T. Xu, M. Jiang, Y. Ling, and Y. Gao, "Crustal structure and deformation beneath eastern and northeastern tibet revealed by P-wave receiver functions," *Earth Planet. Sci. Lett.*, vol. 497, pp. 69–79, Sep. 2018.
[3] V. Tesmer, P. Steigenberger, T. van Dam, and T. Mayer-Gürr, "Vertical deformations from homogeneously processed GRACE and global GPS long-term series," *J. Geodesy*, vol. 85, no. 5, pp. 291–310, May 2011.
[4] C. Braitenberg, "The deforming and rotating Earth—A review of the 18th international symposium on geodynamics and Earth Tide, Trieste 2016," *Geodesy Geodyn.*, vol. 9, no. 3, pp. 187–196, 2018.
[5] W. Feng, M. Zhong, J.-M. Lemoine, R. Biancale, H.-T. Hsu, and J. Xia, "Evaluation of groundwater depletion in north China using the gravity recovery and climate experiment (GRACE) data and ground-based measurements," *Water Resour. Res.*, vol. 49, no. 4, pp. 2110–2118, Apr. 2013.
[6] W. Yin, L. Hu, M. Zhang, J. Wang, and S.-C. Han, "Statistical downscaling of GRACE-derived groundwater storage using ET data in the north China plain," *J. Geophys. Res. Atmos.*, vol. 123, no. 11, pp. 5973–5987, Jun. 2018.
[7] R. Liu, J. Li, H. Fok, C. K. Shum, and Z. Li, "Earth surface deformation in the north China plain detected by joint analysis of GRACE and GPS data," *Sensors*, vol. 14, no. 10, pp. 19861–19876, Oct. 2014.
[8] Y. Pang, H. Zhang, H. Cheng, and Y. Shi, "Changes of crustal stress induces by groundwater over-puming in north China plain," *Chin. J. Geophys.*, vol. 59, no. 4, pp. 1394–1402, 2016.
[9] G. Zheng, H. Wang, T. J. Wright, Y. D. Lou, R. Zhang, W. X. Zhang, C. Shi, J. F. Huang, and N. Wei, "Crustal deformation in the India-Eurasia collision zone from 25 years of GPS measurements: Crustal deformation in Asia from GPS," *J. Geophys. Res. Solid Earth*, vol. 122, no. 13, pp. 9290–9312, 2017.
[10] P. K. Gautam, V. K. Gahalaut, S. K. Prajapati, N. Kumar, R. K. Yadav, N. Rana, and C. P. Dabral, "Continuous GPS measurements of crustal deformation in Garhwal-Kumaun himalaya," *Quaternary Int.*, vol. 462, no. 12, pp. 124–129, Dec. 2017.
[11] B. Zhong, X. Li, J. Chen, Q. Li, and T. Liu, "Surface mass variations from GPS and GRACE/GFO: A case study in southwest China," *Remote Sens.*, vol. 12, no. 11, pp. 1835–1846, 2020.
[12] W. Zheng, Z. Xu, M. Zhong, and M. Yun, "Efficient accuracy improvement of GRACE global gravitational field recovery using a new inter-satellite range interpolation method," *J. Geodyn.*, vol. 53, no. 1, pp. 1–7, Jan. 2012.
[13] Y. Pan, C. Zhang, H. L. Gong, P. J. F. Yeh, Y. Shen, Y. Guo, Z. Huang, and X. Li, "Detection of human-induced evapotranspiration using GRACE satellite observations in the Haihe River basin of China," *Res. Lett.*, vol. 44, no. 1, pp. 190–199, 2017.
[14] W. Q. Li, W. Wang, C. Y. Zhang, Q. Yang, W. Feng, and Y. Liu, "Monitoring groundwater storage variations in the Guanzhong area using GRACE satellite gravity data," *Chin. J. Geophys.*, vol. 61, no. 6, pp. 67–75, 2018.
[15] H. S. Fok and Y. Liu, "An improved GPS-inferred seasonal terrestrial water storage using terrain-corrected vertical crustal displacements constrained by GRACE," *Remote Sens.*, vol. 11, no. 12, p. 1433, Jun. 2019.
[16] M. He, W. Shen, Y. Pan, R. Chen, and G. Guo, "Temporal-spatial surface seasonal mass changes and vertical crustal deformation in south China block from GPS and GRACE measurements," *Sensors*, vol. 18, no. 1, p. 99, 2017.
[17] S. Nahmani, O. Bock, M. N. Bouin, A. Santamaría-Gómez, J. P. Boy, X. Collilieux, L. Métivier, I. Panet, P. Genthon, and C. D. Linage, "Hydrological deformation induced by the west African Monsoon: Comparison of GPS, GRACE and loading models," *J. Geophys. Res. Atmos.*, vol. 117, no. B5, pp. 0148–0227, 2012.
[18] T. Zhang, W. Shen, Y. Pan, and W. Luan, "Study of seasonal and long-term vertical deformation in nepal based on GPS and GRACE observations," *Adv. Space Res. Off. J. Committee Space Res.*, vol. 61, no. 4, pp. 1005–1016, Feb. 2018.
[19] Y. H. Ding, D. F. Huang, Y. L. Shi, Z. S. Jiang, and T. Chen, "Determination of vertical surface displacements in Sichuan using GPS and GRACE measurements," *Chin. J. Geophys.*, vol. 61, no. 12, pp. 4777–4788, 2018.
[20] A. Klos, M. A. Karegar, J. Kusche, and A. Springer, "Quantifying noise in daily GPS height time series: Harmonic function versus GRACE-assimilating modeling approaches," *IEEE Geosci. Remote Sens. Lett.*, early access, Apr. 8, 2020, doi: 10.1109/LGRS.2020.2983045.
[21] T. Qiao, J. Ren, Z. Wang, J. Zabalza, M. Sun, H. Zhao, S. Li, J. A. Benediktsson, Q. Dai, and S. Marshall, "Effective denoising and classification of hyperspectral images using curvelet transform and singular spectrum analysis," *IEEE Trans. Geosci. Remote Sens.*, vol. 55, no. 1, pp. 119–133, Jan. 2017.
[22] J. L. Davis, "Climate-driven deformation of the solid Earth from GRACE and GPS," *Geophys. Res. Lett.*, vol. 31, no. 24, 2004, Art. no. L24605.

[23] N. E. Huang, Z. Shen, S. R. Long, M. C. Wu, H. H. Shih, Q. Zheng, N.-C. Yen, C. C. Tung, and H. H. Liu, "The empirical mode decomposition and the Hilbert spectrum for nonlinear and non-stationary time series analysis," *Proc. Roy. Soc. London. A, Math., Phys. Eng. Sci.*, vol. 454, no. 1971, pp. 903–995, Mar. 1998.
[24] T. Wang, M. Zhang, Q. Yu, and H. Zhang, "Comparing the application of EMD and EEMD on time-frequency analysis of seimic signal," *J. Appl. Geophys.*, vol. 83, no. 1, pp. 29–34, 2012.
[25] C. Liu, L. Zhu, and C. Ni, "The chatter identification in end milling based on combining EMD and WPD," *Int. J. Adv. Manuf. Technol.*, vol. 91, nos. 9–12, pp. 3339–3348, Aug. 2017.
[26] J. D. Zheng, J. S. Cheng, and Y. Yang, "Modified EEMD algorithm and its applications," *J. Vib.*, vol. 32, no. 21, pp. 21–26 and 46, 2013.
[27] J. Wang, X. He, and V. Ferreira, "Ocean wave separation using CEEMD-wavelet in GPS wave measurement," *Sensors*, vol. 15, no. 8, pp. 19416–19428, Aug. 2015.
[28] Y. Li, L. Yaan, X. Chen, and J. Yu, "Denoising and feature extraction algorithms using NPE combined with VMD and their applications in ship-radiated noise," *Symmetry*, vol. 9, no. 11, pp. 256–265, Nov. 2017.
[29] Y. Yao, S. Sfarra, C. Ibarra-Castanedo, R. You, and X. P. V. Maldague, "The multi-dimensional ensemble empirical mode decomposition (MEEMD)," *J. Thermal Anal. Calorimetry*, vol. 128, no. 3, pp. 1841–1858, Jun. 2017.
[30] H. Liu, J. Jing, and J. Ma, "Fault diagnosis of electromechanical actuator based on VMD multifractal detrended fluctuation analysis and PNN," *Complexity*, vol. 2018, pp. 1–11, Aug. 2018.
[31] X. Li and C. Li, "Pretreatment and wavelength selection method for near-infrared spectra signal based on improved CEEMDAN energy entropy and permutation entropy," *Entropy*, vol. 19, no. 7, p. 380, Jul. 2017.
[32] W. Deng, H. Zhao, X. Yang, and C. Dong, "A fault feature extraction method for motor bearing and transmission analysis," *Symmetry*, vol. 9, no. 5, p. 60, Apr. 2017.
[33] M. M. Rahman, M. I. H. Bhuiyan, and A. B. Das, "Classification of focal and non-focal EEG signals in VMD-DWT domain using ensemble stacking," *Biomed. Signal Process. Control*, vol. 50, pp. 72–82, Apr. 2019.
[34] Z. Chen, Y. Li, R. Cao, W. Ali, J. Yu, and H. Liang, "A new feature extraction method for ship-radiated noise based on improved CEEMDAN, normalized mutual information and multiscale improved permutation entropy," *Entropy*, vol. 21, no. 6, p. 624, Jun. 2019.
[35] S. Zhang, H. Liu, M. Hu, A. Jiang, L. Zhang, F. Xu, and G. Hao, "An adaptive CEEMDAN thresholding denoising method optimized by nonlocal means algorithm," *IEEE Trans. Instrum. Meas.*, vol. 69, no. 9, pp. 6891–6903, Sep. 2020.
[36] K. Dragomiretskiy and D. Zosso, "Variational mode decomposition," *IEEE Signal Process. Soc.*, vol. 62, no. 3, pp. 531–544, Feb. 2014.
[37] Y. Li, Y. Li, X. Chen, and J. Yu, "Research on ship-radiated noise denoising using secondary variational mode decomposition and correlation coefficient," *Sensors*, vol. 18, no. 2, p. 48, Dec. 2017.
[38] Y.-F. Sang, Z. Wang, and C. Liu, "Period identification in hydrologic time series using empirical mode decomposition and maximum entropy spectral analysis," *J. Hydrol.*, vols. 424–425, pp. 154–164, Mar. 2012.
[39] Z. Qu, W. Feng, and H.-F. Liang, "Periodicity of the solar radius revisited by using empirical mode decomposition and the Lomb-Scargle method," *Res. Astron. Astrophys.*, vol. 15, no. 6, pp. 879–888, May 2015.
[40] R. Liu, R. Zou, J. Li, C. Zhang, B. Zhao, and Y. Zhang, "Vertical displacements driven by groundwater storage changes in the north China plain detected by GPS observations," *Remote Sens.*, vol. 10, no. 2, pp. 259–272, 2018.
[41] G. Blewitt, D. Lavallée, P. Clarke, and K. Nurutdinov, "A new global mode of Earth deformation: Seasonal cycle detected," *Science*, vol. 294, no. 5550, pp. 2342–2345, Dec. 2001.
[42] Y. Xiang, J. Yue, K. Cong, Y. Xing, and D. Cai, "Characterizing the seasonal hydrological loading over the asian continent using GPS, GRACE, and hydrological model," *Pure Appl. Geophys.*, vol. 176, no. 11, pp. 5051–5068, Nov. 2019.
[43] M. Cheng, B. D. Tapley, and J. C. Ries, "Deceleration in the Earth's oblateness," *J. Geophys. Res. Solid Earth*, vol. 118, no. 2, pp. 740–747, Feb. 2013.
[44] S. Swenson, D. Chambers, and J. Wahr, "Estimating geocenter variations from a combination of GRACE and ocean model output," *J. Geophys. Res. Solid Earth*, vol. 113, no. B8, pp. 1–8, Aug. 2008.
[45] T. van Dam, J. Wahr, and D. Lavallée, "A comparison of annual vertical crustal displacements from GPS and gravity recovery and climate experiment (GRACE) over Europe," *J. Geophys. Res.*, vol. 112, no. B3, pp. 404–415, 2007.
[46] E. Lantz, C. E. Calosso, E. Rubiola, V. Giordano, C. Fluhr, B. Dubois, and F. Vernotte, "KLTS: A rigorous method to compute the confidence intervals for the three-cornered hat and for groslambert covariance," *IEEE Trans. Ultrason., Ferroelectr, Freq. Control*, vol. 66, no. 12, pp. 1942–1949, Dec. 2019.
[47] H. Li, Q. Lin, Q. Wang, Q. Liu, and J. Wu, "Research on spectrum denoising methods based on the combination of wavelet package transformation and mathematical morphology," *Spectrosc. Spectral Anal.*, vol. 30, no. 3, pp. 644–648, 2010.
[48] S.-H. Kong, "Fast multi-satellite ML acquisition for A-GPS," *IEEE Trans. Wireless Commun.*, vol. 13, no. 9, pp. 4935–4946, Sep. 2014.
[49] J.-C. Yoo, B. D. Choi, and H.-K. Choi, "1-D fast normalized cross-correlation using additions," *Digit. Signal Process.*, vol. 20, no. 5, pp. 1482–1493, Sep. 2010.
[50] K. M. Larson and E. E. Small, "Estimation of snow depth using l1 GPS signal-to-noise ratio data," *IEEE J. Sel. Topics Appl. Earth Observ. Remote Sens.*, vol. 9, no. 10, pp. 4802–4808, Oct. 2016.
[51] T. Zan, Z. Pang, M. Wang, and X. Gao, "Research on Early fault diagnosis of rolling bearing based on VMD," in *Proc. CMAME*, 2018, pp. 41–45.
[52] C. Ji, Y. Shen, and Q. Wang, "Baseline time series noise analysis of IGS reference stations in Chinese mainland," *J. Navigat. Positioning*, vol. 27, no. 3, pp. 108–114, 2019.
[53] Q. Chen, T. van Dam, N. Sneeuw, X. Collilieux, M. Weigelt, and P. Rebischung, "Singular spectrum analysis for modeling seasonal signals from GPS time series," *J. Geodyn.*, vol. 72, no. 12, pp. 25–35, Dec. 2013.
[54] E. Gülal, H. Erdoğan, and İ. Tiryakioğlu, "Research on the stability analysis of GNSS reference stations network by time series analysis," *Digit. Signal Process.*, vol. 23, no. 6, pp. 1945–1957, Dec. 2013.
[55] C. Chen, R. Zou, and R. L. Liu, "Vertical deformation of seasonal hydrological loading in southern tibet detected by joint analysis of GPS and GRACE," *Geomatics Inf. Sci. Wuhan Univ.*, vol. 43, no. 5, pp. 669–675, 2018.
[56] Y. Fu and J. T. Freymueller, "Seasonal and long-term vertical deformation in the nepal himalaya constrained by GPS and GRACE measurements," *J. Geophys. Res. Solid Earth*, vol. 117, no. B3, pp. 487–497, Mar. 2012.
[57] Q. Zhao, B. Zhang, Y. Yao, W. Wu, G. Meng, and Q. Chen, "Geodetic and hydrological measurements reveal the recent acceleration of groundwater depletion in north China plain," *J. Hydrol.*, vol. 575, no. 22, pp. 1065–1072, Aug. 2019.
[58] R. Schmidt, F. Flechtner, U. Meyer, K.-H. Neumayer, C. Dahle, R. König, and J. Kusche, "Hydrological signals observed by the GRACE satellites," *Surv. Geophys.*, vol. 29, nos. 4–5, pp. 319–334, Oct. 2008.
[59] S. Bruinsma and J. Forbes, "Anomalous behavior of the thermosphere during solar minimum observed by CHAMP and GRACE," *J. Geophys. Res. Space Phys.*, vol. 115, no. A11, pp. 13–23, 2010.
[60] D. Long, L. Longuevergne, and B. R. Scanlon, "Uncertainty in evapotranspiration from land surface modeling, remote sensing, and GRACE satellites," *Water Resour. Res.*, vol. 50, no. 2, pp. 1131–1151, Feb. 2014.

YIFAN SHEN received the master's degree in surveying and mapping engineering from Liaoning Technical University, China, in 2019. He is currently pursuing the joint Ph.D. degree with the Qian Xuesen Laboratory of Space Technology, China Academy of Space Technology. His research interests include satellite gravity, data assimilation, crustal deformation, and time series analysis.

WEI ZHENG received the Ph.D. degree from the College of Physics, Huazhong University of Science and Technology, in 2007. From 2007 to 2015, he worked as an Associate Research Fellow with the Institute of Geodesy and Geophysics, Chinese Academy of Sciences. Since 2015, he has been working with the Qian Xuesen Laboratory of Space Technology, China Academy of Space Technology, as a Research Fellow. His research interests include satellite gravity, underwater integrated navigation, satellite sea surface altimetry, and satellite navigation.

WENJIE YIN received the Ph.D. degree from the College of Water Sciences, Beijing Normal University, in 2019. Since 2019, he has been working with the Qian Xuesen Laboratory of Space Technology, China Academy of Space Technology, as a Research Fellow. His research interests include satellite gravity, data assimilation, and climate change.

AIGONG XU received the Ph.D. degree from Wuhan University, China, in 1998. From 1999 to 2000, he engaged in postdoctoral research with Tongji University. From 2001 to 2003, he worked as a Research Fellow with Nanyang Polytechnic University, Singapore. Since 2003, he has been working with Liaoning Technical University, as a Professor. His research interests include BDS/GPS high precision positioning algorithm, surface subsidence, indoor positioning, and satellite gravity.

HUIZHONG ZHU received the Ph.D. degree from Wuhan University, China, in 2012. Since 2012, he has been working as an Associate Professor with Liaoning Technical University. His research interests include BDS/GPS high precision positioning algorithm and data processing of BDS/GPS.